nature communications

Article

https://doi.org/10.1038/s41467-025-58352-x

Photoluminescent delocalized excitons in donor polymers facilitate efficient charge generation for high-performance organic photovoltaics

Received: 11 October 2024

Accepted: 20 March 2025

Published online: 03 April 2025

Check for updates

Kui Jiang[1,11], Robert J. E. Westbrook[2,11], Tian Xia[3], Cheng Zhong[4], Jianxun Lu[5], Azzaya Khasbaatar[6], Kaikai Liu[3], Francis R. Lin[1,3,7] ✉, Sei-Hum Jang[8], Jie Zhang[9], Yuqing Li[5], Ying Diao[6], Zhanhua Wei[5], Hin-Lap Yip[3,7,10], David S. Ginger[2] ✉ & Alex K.-Y. Jen[1,3,7,8,10] ✉

Efficient delocalization of photo-generated excitons is a key to improving the charge-separation efficiencies in state-of-the-art organic photovoltaic (OPV) absorber. While the delocalization in non-fullerene acceptors has been widely studied, we expand the scope by studying the properties of the conjugated polymer donor D18 on both the material and device levels. Combining optical spectroscopy, X-ray diffraction, and simulation, we show that D18 exhibits stronger π−π interactions and interchain packing compared to classic donor polymers, as well as higher external photoluminescence quantum efficiency (~26%). Using picosecond transient absorption spectroscopy and streak camera photoluminescence measurements, we show that the initial D18 excitons form delocalized intermediates, which decay radiatively with high efficiency in neat films. In single-component OPV cells based on D18, these intermediate excitations can be harvested with an internal quantum efficiency >30%, while in blends with acceptor Y6 they provide a pathway to free charge generation that partially bypasses performance-limiting charge-transfer states at the D18:Y6 interface. Our study demonstrates that donor polymers can be further optimized using similar design strategies that have been successful for non-fullerene acceptors, opening the door to even higher OPV efficiencies.

Organic photovoltaics (OPVs) differ from inorganic photovoltaics in that the primary photo-excitations in OPVs are typically excitons with binding energies exceeding k_bT[1,2]. This excitonic character stems from their low dielectric constants as compared to inorganic semiconductors such as silicon or perovskites[3]. As such, efficient OPVs usually consist of a donor-acceptor blend, wherein the energetic separation between their frontier molecular orbitals provides a driving force to overcome the Coulomb binding energy of the exciton (E_b)[4], along with entropic factors[5–7]. In the general picture (Supplementary Fig. 1), photo-excitations initially consist of singlet local excitons (^{1}LE) on the donor that then diffuse to an interface with the acceptor (or vice versa), whereupon they dissociate into free charges (FC) with interfacial charge-transfer (CT) excitons as intermediates. The recombination of FC occurs also via interfacial CTs, with an electron on the acceptor and a hole on the donor. During recombination, these CT excitons presumably re-form in a 3:1 ratio of spin-triplet (^{3}CT) and spin-singlet (^{1}CT) states via spin-statistical non-geminate recombination[8]. The low radiative

A full list of affiliations appears at the end of the paper. ✉e-mail: franclin@cityu.edu.hk; dginger@uw.edu; alexjen@cityu.edu.hk

efficiency of such recombination leads to voltage and current loss, ultimately limiting OPV efficiency[9–11].

Given that CT states are critical to both charge separation and recombination, many strategies for improving OPV efficiency center around manipulating them. Examples include improving radiative efficiency in CT states via CT-LE hybridization[11], improving CT state order[12], and controlling CT state concentration altogether[13,14]. Additionally, it has been widely reported that charge carrier delocalization associated with intimate packing in PCBM[15], and later non-fullerene acceptors (NFAs)[16–19], leads to ultrafast ionization of CT states. Furthermore, solid-state interactions in neat NFAs and other small molecules may facilitate the formation of highly delocalized excitons[17,20–24], with improved radiative efficiency[18,22]. These delocalized excitons have been proposed to supplant the formation of interfacial donor-acceptor CT states. Nonetheless, the relationship between delocalization and radiative efficiency in donors, and their role in affecting the final OPV performance, have been less studied.

In this work, we observe the photoluminescence associated with delocalized excitons in the neat films of conjugated polymer D18, a high-performance donor for state-of-the-art OPVs. This photoluminescence stems from the solid-state packing of D18, where strongly interacting annulated benzothiadiazoles strengthen interchain π-communication and facilitate exciton delocalization. We investigate the link between exciton delocalization and performance in OPV cells adopting different donors and show that photon-to-current conversion (i.e., internal/external quantum efficiency (IQE/EQE)) benefits from a stronger delocalization character. Specifically, exciton delocalization in the D18 component of OPV blends offers a distinct pathway to generate free carriers (FC), which bypasses the formation of interfacial CT states during electron transfer to realize a power conversion efficiency (PCE) of over 19%. Our study provides a framework for understanding how intimate intermolecular interactions help overcome the local excitonic character in organics to facilitate FC generation, thus improving OPV efficiency. Engineering delocalization in organic semiconductors will maximize their exciton dissociation efficiency and minimize terminal back recombination, important steps towards the further development of OPVs.

Results

Photoluminescence from a delocalizing polymer

The donor polymer D18 has been widely adopted in state-of-the-art high-performance OPVs to show very efficient photon-to-current conversion (i.e., high short-circuit current density (J_{SC}))[25–27], despite its infamous processibility challenges due to limited solubility and high viscosity[28]. From this observation, we began to consider the relationship between chemical structure, aggregation, and charge separation in OPV blends based on D18 and other well-known donor polymers such as P3HT and PM6 (Fig. 1a). P3HT is a homopolymer of 3-hexylthiophene, whereas PM6 and D18 are alternating push-pull copolymers with identical electron-donating (D; BDT) but different electron-withdrawing (A; BDD/DTBT for PM6/D18) moieties. These structures directly result in different push-pull strengths that shift the polymer frontier molecular orbital energetics (Supplementary Fig. 2). Moreover, the heteroatoms with different electronegativities in these moieties help establish versatile non-covalent interactions that modulate the communications between polymer chains, which may impact exciton delocalization.

We use computation to evaluate the strength of the intermolecular interactions that contribute to exciton delocalization (Supplementary Note 1, Supplementary Tables 1–3, and Supplementary Figs. 3 and 4). The stronger interactions between BDT, BDD, and DTBT moieties in PM6 and D18 help establish intimate π-interactions between polymer chains[29,30], significantly lowering the electron-hole overlap in PM6 and D18 relative to P3HT. We find that D18 has the lowest electron-hole overlap of all, most likely because the interactive DTBT unit is free of alkyl chains, reducing the amount of steric hindrance that would otherwise impede communication between polymer π-backbones. These results echo with previous findings that D18 films show high crystallinity with improved long-range order[28]. Such close packing facilitates through-space conjugation between D18 chains, promoting exciton delocalization to partition excited-state energy.

Next, we explore experimental evidence supporting the formation of π-interacting aggregates by using steady-state absorption and photoluminescence (PL) spectroscopy (Fig. 1b, and Supplementary Fig. 5). The absorption of the P3HT film shows a low-energy 0–0 vibronic shoulder (~600 nm), while PM6 and D18 both show more intense 0–0 peaks (611/580 nm for PM6/D18) than 0–1 peaks (575/545 nm for PM6/D18). This difference in peak ratios implies that the microstructure in PM6 and D18 films is more ordered than that of P3HT[31,32]. Regarding the emission spectra, D18 shows the narrowest steady-state photoluminescence peak and smallest Stokes shift compared to P3HT and PM6, which is again consistent with improved order in D18 films. We next measure the photoluminescence quantum yield (PLQY), where we strikingly find D18 to be much more luminescent (PLQY = 26%) than P3HT and PM6 (both PLQY < 10%). The PLQY of D18 is the highest so far among polymer donors used for high-efficiency OPVs[33], especially given that luminescence can be quenched in D-A copolymers having strong intramolecular CT character[34]. We also explore the potential of D18 as an emitter and achieve an electroluminescence EQE of 1.23% in a light-emitting diode (Supplementary Fig. 6).

To better understand the correlation between the extent of aggregation and luminescent properties, we perform temperature-dependent steady-state photoluminescence measurements of D18 in diluted solution (Fig. 1e). We observe a gradual blue-shift of the D18 PL spectrum as the temperature is increased, consistent with the disaggregation of D18 at elevated temperatures. The lower-energy peak (695 nm) from D18 aggregates in solution matches the feature in the thin-film photoluminescence spectrum, where the higher-energy peak (~575 nm) associated with fully disaggregated D18 chains is absent. This analysis helps explain that the D18 thin-film photoluminescence is associated with the aggregation of D18 in the condensed phase, and the aggregation of D18 is strong enough to be maintained even at low concentrations in a solvating environment. In contrast, the characteristic peak in the PM6 thin-film photoluminescence profile (755 nm) is hardly maintained when in diluted solution even at room temperature, while those of P3HT are fully eliminated in solution (Fig. 1c, d). We further utilize small-angle X-ray scattering measurements on a D18 solution to confirm the existence of semicrystalline fiber aggregates with strong interchain interactions in solution, which is consistent with the high crystallinity of solution-processed thin films (Supplementary Note 2, and Supplementary Fig. 7). Together, these experiments indicate that D18 is unique in supporting unusually low levels of non-radiative recombination in an unusually ordered donor polymer.

Interplay between aggregation and exciton delocalization

We investigate the photophysics of the *neat* D18 films with transient absorption (TA) and photoluminescence spectroscopy (Fig. 2, and Supplementary Figs. 8–13) to elucidate the link between aggregation and excited states in D18. Upon excitation, we observe a bleach at 590 nm and photoinduced absorption (PIA) at 1170 nm, which we attribute to the ground-state bleach (GSB_{D18}) and local exciton ($^1LE_{D18}$) of D18, respectively (Fig. 2a)[13]. The $^1LE_{D18}$ feature decays with fast biexponential kinetics with a fast (2.3 ps) and slower (55 ps) decay constant (Fig. 2b). Concurrent with the decay of $^1LE_{D18}$, we observe new PIA features grow in at 650 nm and 800 nm on a similar timescale (2.7 ps) as the fast $^1LE_{D18}$ decay. The 650 nm and 800 nm features have similar kinetics, suggesting they come from the same excited state.

https://doi.org/10.1038/s41467-025-58352-x

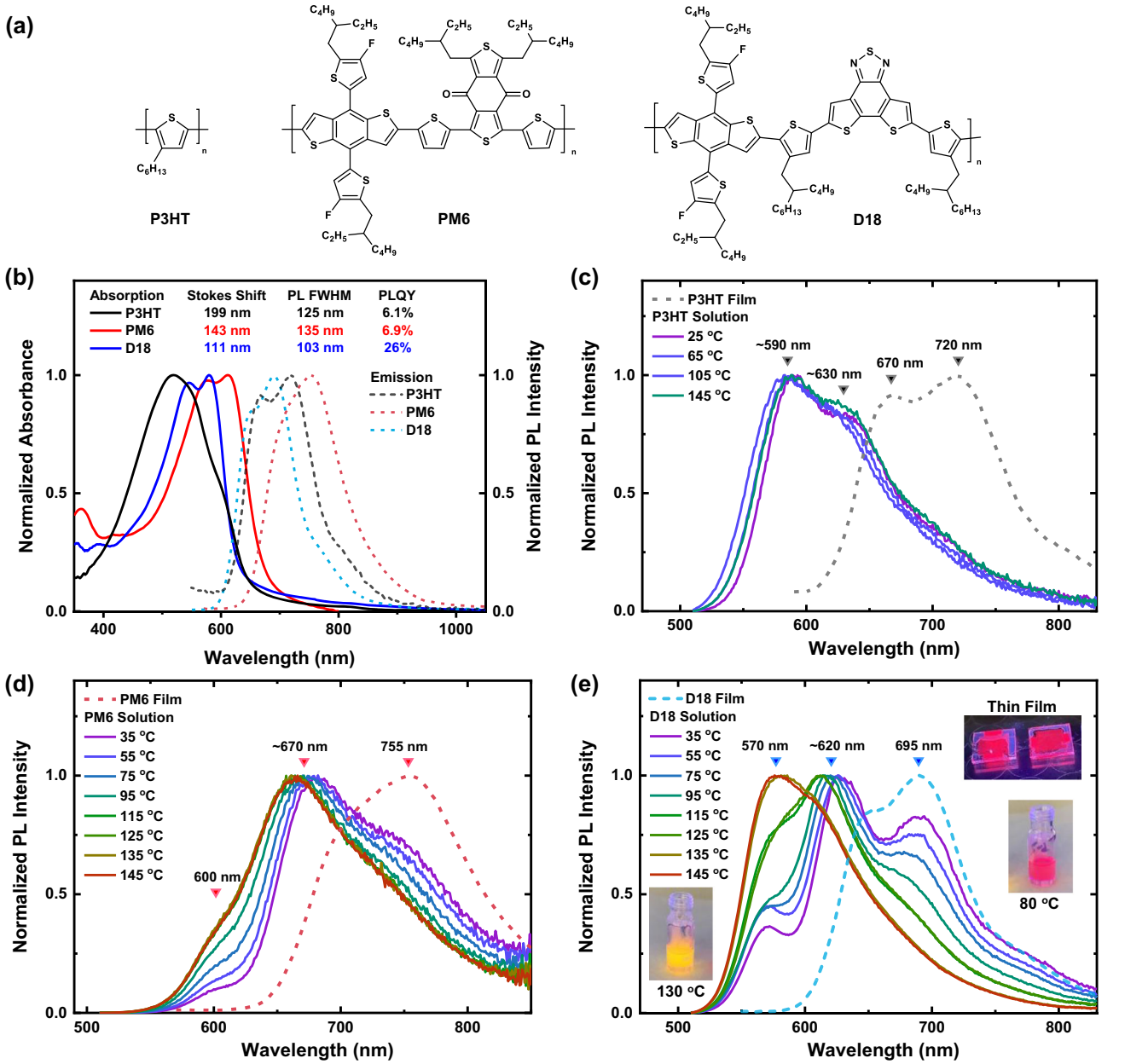

Fig. 1 | The chemical structures and optical properties of P3HT, PM6, and D18. **a** Chemical structures of polymers. **b** Normalized thin-film absorption (solid curves) and emission (dashed curves, excited at 365 nm) profiles. The values of the Stokes shift (defined by the spectral shift between the absorption and emission maxima), the full width at half maximum (FWHM) of the emission peak, and the PLQY are included. **c**–**e** Normalized temperature-dependent photoluminescence profiles (solid lines, excited at 365 nm) of (**c**) P3HT, (**d**) PM6, and (**e**) D18 solutions (10 μg/mL in *o*-DCB) in the range up to 145 °C. The thin-film emission profiles (dash lines) are included for comparison. The inset figures in (**e**) show images of the emission from the D18 thin films (room temperature) and heated solutions (at 80 °C and 130 °C, respectively).

Notably, the 650 nm feature shape is a close match with the first derivative of the ground-state absorption of D18 (Supplementary Fig. 10), as the electric field between separating charges can lead to derivative-like modulation of the ground-state absorption via the Stark effect[15]. We also find that the 650 nm and 800 nm features match closely with the D18 hole polaron as determined by hole doping experiments (Supplementary Fig. 11).

Given these similarities, the similarity between the 650 nm and 800 nm features and the D18 hole polaron could be evidence for free charges or a delocalized singlet exciton (see Supplementary Note 3 for a discussion of nomenclature). These two types of excited states are difficult to distinguish, because a hole wavefunction in $^1D_{D18}$ may be sufficiently separated from that of the electron, such that its spectrum resembles that of a fully dissociated hole polaron[35]. We further note that the decay of the 650 nm and 800 nm TA features can be fit to a single exponential, which has a fluence-independent lifetime at low fluence (Supplementary Fig. 12). This behavior is more consistent with bound states than free polarons, which tend to give higher-order kinetics. We therefore attribute the EA signal in neat D18 films to a delocalized singlet exciton ($^1D_{D18}$). We suggest the delocalization of this state is facilitated by the interactive DTBT unit, which can strengthen interchain communication between D18 backbones in aggregates. We further support this view via measurements in solution, where we show that the electroabsorption feature diminishes in intensity after disaggregation at higher temperatures (Supplementary Fig. 13).

https://doi.org/10.1038/s41467-025-58352-x

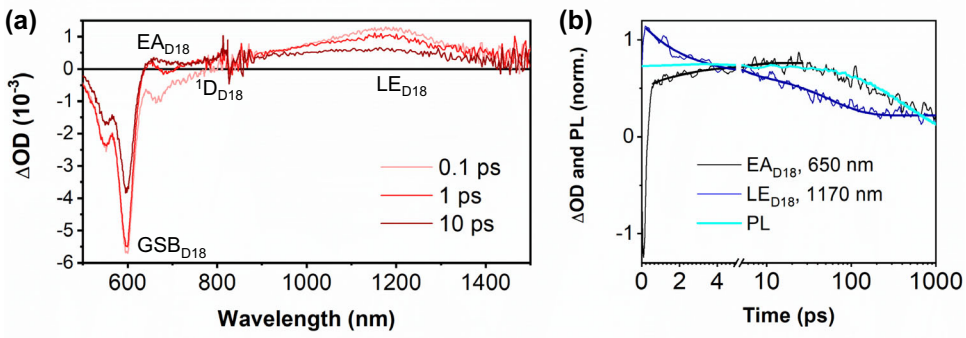

Fig. 2 | Transient optical characterization of neat D18. a Selected TA spectra at different times from a neat D18 sample with key features indicated (GSB_{D18} = ground-state bleach, $^1LE_{D18}$ = D18 local exciton, $^1D_{D18}$ = delocalized exciton, EA_{D18} = electroabsorption peak). **b** Normalized transient absorption decays of the D18 local exciton ($^1LE_{D18}$, 1170 nm) and electroabsorption (EA_{D18}, 650 nm) features overlaid with the PL decay as acquired from the streak camera of the same film. The D18 film was excited at 550 nm with a fluence of 2 μJ/cm^2 in all cases.

Given that better delocalization of excitons should increase the exciton diffusion length (L_{exc})[36], we compared L_{exc} for D18, P3HT, and PM6 using the exciton-exciton annihilation method[37–39]. Using this methodology, we estimate D18 to have an L_{exc} of 16 nm, significantly longer than in P3HT (~8 nm) and PM6 (~7 nm). We propose that the larger L_{exc} in D18 is due to better delocalization across more molecules due to denser packing in aggregates. This delocalizing character in D18 distinguishes it from many other strongly aggregating conjugated polymers such as PffBT4T-2OD, where bulky aliphatic substituents affect interchain interactions (Supplementary Note 4, Supplementary Figs. 14–17)[40–42].

Next, we consider the neat photoluminescence decay kinetics of D18. Importantly, the photoluminescence lifetime of aggregates in the D18 film (i.e., at ~695 nm, Supplementary Fig. 18) from streak camera measurements more closely follows the decay of the $^1D_{D18}$ (and EA_{D18}) states from TA measurements than the decay of promptly formed $^1LE_{D18}$ (Fig. 2b). The match between the $^1D_{D18}$ and PL decay provides strong evidence for the formation of a luminescent delocalized exciton in D18 aggregates as the dominant luminescent species in neat D18 films, likely because the strong π-stacking between D18 chains facilitates exciton delocalization. Given the high luminescence nature of D18, we propose there is a connection between the high PLQY and efficient exciton delocalization in D18. This result would echo recent reports on near-infrared organometallic emitters, where increasing the extent of exciton delocalization through intimate molecular packing in the condensed phase improves the PLQY[22], as well as reports that attribute the high PLQY in Y6 to limited exciton-vibration coupling (and thus reduced non-radiative recombination) arising from delocalized excitons[18].

Higher PCE due to enhanced photon-to-current conversion

We fabricate OPV cells using *neat* P3HT, PM6, and D18 as the active layer to evaluate how the extent of delocalization can be associated with photon-to-current conversion efficiency (Fig. 3, and Supplementary Table 4). We introduce a fullerene-derived self-assembled monolayer, C60-G4PA, to modify the work function of ITO substrate for better electron extraction (Supplementary Note 5, and Supplementary Figs. 19–23). Interestingly, we achieve a PCE of 2.00 ± 0.05% from neat D18 cells with average IQE > 25% across the photoresponse (peak IQE 30.4%, 540 nm). The PM6 cells show a lower average IQE (peak IQE 24.1%, 565 nm), but similar overall PCE (1.88 ± 0.17%) due to their broader absorption, while P3HT cells only show both a lower peak IQE of 20.4% (450 nm) and lower total PCE of 0.56 ± 0.08%. The higher IQE/EQE responses from D18 cells indicate more efficient photocurrent generation than in those based on P3HT and PM6 (Supplementary Fig. 21). The trend in the IQE/EQE data is in qualitative agreement with the exciton diffusion lengths extracted in each case, which increase in the order P3HT (~8 nm) <PM6 (~7 nm) <D18 (~16 nm).

Given the prevalence of CT state formation in bilayer architectures[43,44], we compared CT state formation in the single-component cells (ITO/C60-G4PA/D18/MoO_3/Ag) and binary cells (ITO/C60-G4PA/D18:PCBM bulk heterojunction/MoO_3/Ag) with electroluminescence (EL) characterization. In the binary cells, we observe an EL peak at 1.36 eV (Fig. 3c), consistent with the formation of a CT state with sub-bandgap energy. In the single-component cells, we see a small contribution from a state at similar energy (~1.33 eV), which we attribute to the formation of some CT states at the C60-G4PA/D18 interface. However, the predominant EL feature here is at higher energy (~1.8 eV) and matches the EL spectrum of aggregated D18 films, which we have already established comes from the $^1D_{D18}$ state. Therefore, this experiment suggests that while CT states may be formed at the C60-G4PA/D18 interface in our single-component cells, the $^1D_{D18}$ state provides an alternative charge generation pathway, bypassing the losses of the CT state. We corroborate this hypothesis via TA measurements on ITO/C60-G4PA/D18 samples, where the kinetics and spectral features are broadly consistent with neat D18 samples (Supplementary Note 6, and Supplementary Figs. 24–26).

Next, we introduce Y6 as the acceptor to fabricate binary OPV cells (Supplementary Table 5). The resulting D18:Y6 (PCE = 17.56 ± 0.29%) and PM6:Y6 (PCE = 16.08 ± 0.31%) cells show comparable V_{OC}s and fill factors (FFs), but a higher J_{SC} of 27.70 ± 0.56 mA/cm^2 from D18:Y6 compared to that of PM6:Y6 (25.47 ± 0.31 mA/cm^2). Meanwhile, P3HT:Y6 cells have a much lower PCE (1.90 ± 0.11%) with low V_{OC} (0.335 ± 0.007 V), J_{SC} (12.70 ± 0.56 mA/cm^2) and FF (44.64 ± 0.76%). These photovoltaic parameters are consistent with literature reports[45–47]. The trend of V_{OC}s generally matches with the ionization potential offsets between different polymers and Y6 (Supplementary Fig. 2)[48]. However, there is a clear increase in J_{SC} in the order P3HT < PM6 < D18 despite these OPV composites having similar bandgaps. We also measure IQE spectra (Fig. 3e), where the peak response corresponding to polymer absorption (400–600 nm) grows in the sequence of P3HT:Y6 (IQE_{520} = 45.0%), PM6:Y6 (IQE_{540} = 95.8%), D18:Y6 (IQE_{520} = 98.5%), showing the most efficient photon-to-current conversion in the D18:Y6 cells. Furthermore, we improve the photovoltaic performance of D18-based cells to 19.2% by employing a ternary blend consisting of two Y6-derived acceptors, T9TBO-F and Y6-O (Supplementary Figs. 27 and 28). One D18:T9TBO-F:Y6-O ternary cell was certified through asymptotic scans at a PCE of 17.7% representing the quasi-steady-state cell performance (Supplementary Fig. 29).

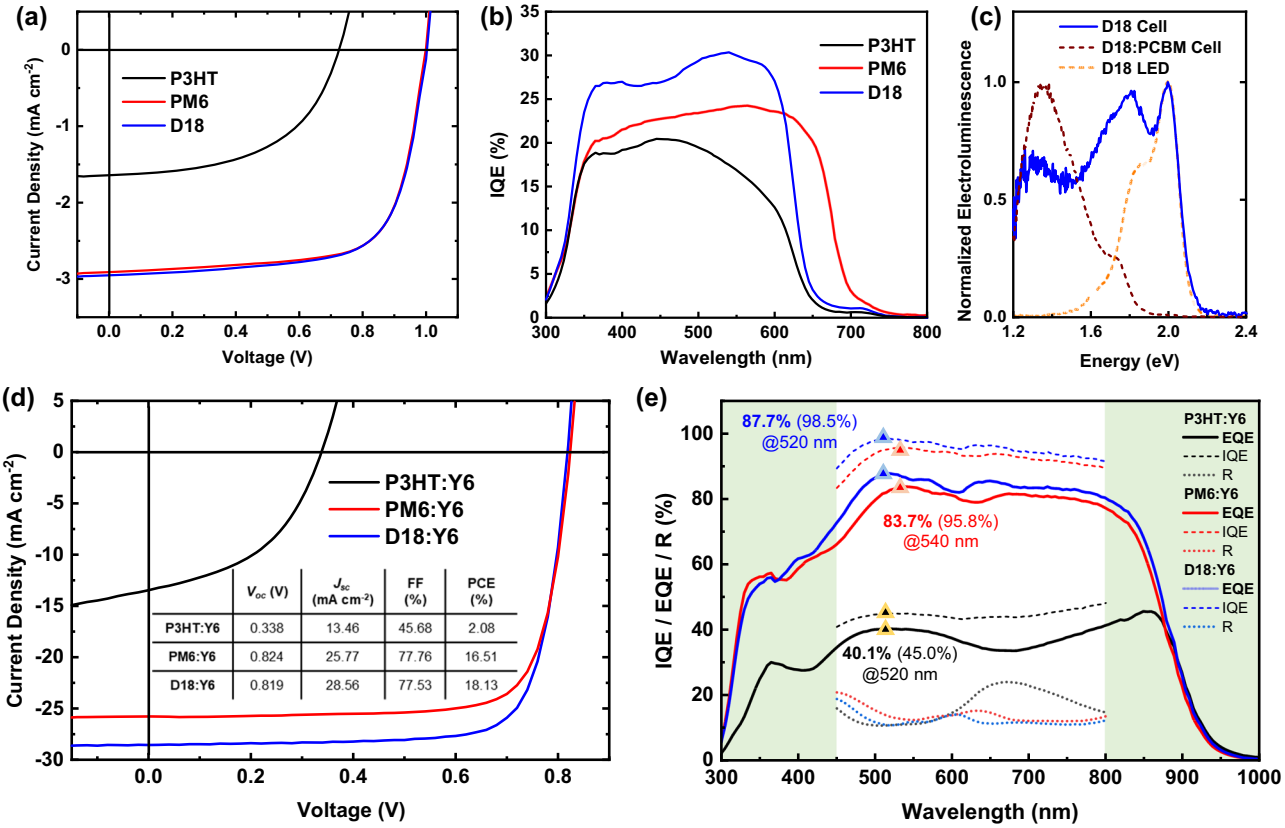

Fig. 3 | The photovoltaic characteristics of OPV cells. a The *J*–*V* profiles of OPV cells with neat polymer active layers, and **b** the corresponding IQE spectra. **c** The electroluminescence profiles of OPV cells having an active layer of neat D18 and D18:PCBM, as well as that from a D18 light-emitting diode. **d** The *J*–*V* profiles of champion P3HT:Y6, PM6:Y6, and D18:Y6 binary OPV cells. The inset table shows the performance of champion devices. **e** The EQE (solid curve) and IQE (dash curve) spectra, and the surface reflectance (R, dot curve) as a function of wavelength for P3HT:Y6, PM6:Y6, and D18:Y6 OPV cells. The values and corresponding wavelengths of peak EQE (*and IQE in the brackets*) in the corresponding donor absorption region are included.

Delocalization in donor affects carrier generation pathways

We next explore the charge-separation mechanism in the D18:Y6 blend using TA measurements (Fig. 4). We provide detailed characterization of D18:Y6 pumped at wavelengths that selectively excite Y6 in Supplementary Figs. 30–32 and Supplementary Note 7. Here, we focus on D18:Y6 pumped at 550 nm for preferential D18 excitation.

Immediately upon photoexciting at 550 nm (~0.1 ps), we observe the $^1LE_{D18}$, GSB_{D18}, EA_{D18}, and Y6 local exciton ($^1LE_{Y6}$) states at ~1200 nm, ~595 nm, ~630 nm, and ~900 nm respectively (Fig. 4a, b). We also note that the initial signal from $^1LE_{D18}$ is significantly quenched in the D18:Y6 blend compared to neat D18 (Supplementary Fig. 33), and EA_{D18} (associated with $^1D_{D18}$) is fully formed, consistent with rapid (<0.2 ps) transfer from $^1LE_{D18}$ to $^1D_{D18}$. Importantly, the EA_{D18} signal exists at ~0.1 ps, before the maxima in GSB_{Y6} and A^-_{Y6} are reached (~1 ps), suggesting that charge separation begins in the D18 moiety prior to electron transfer to Y6. Given that there is no rise in the EA_{D18} feature after ~1 ps, and that the decay of EA_{D18} in this time range is intensity dependent (Supplementary Fig. 34), we infer that separated charges have been formed within ~1 ps, and attribute the remaining EA_{D18} decay to non-geminate recombination of charges fully separated across the D18:Y6 interface. All of this evidence points to the direct electron transfer from the $^1D_{D18}$ state to energetically downhill free charge ($FC_{D18:Y6}$) states. Delocalized states have been reported to exhibit faster charge transfer in several previous reports[15,16,49,50].

Given the significance of energy transfer from donor to acceptor in some OPV systems[51,52], we also consider, but rule out, a dominant role for energy transfer in D18:Y6 charge generation kinetics. In a Förster resonance energy transfer event, a (virtual) photon would be emitted by a D18 exciton and re-absorbed in the Y6 moiety of the blend. As such, in this case, the TA dynamics should slow to match those in which Y6 is preferentially excited (Supplementary Fig. 31). However, we find that FC is formed more quickly (~1 ps) following direct photoexcitation of D18 than direct photoexcitation of Y6 (~4 ps). We therefore conclude that electron transfer to Y6 is the primary charge generation process in D18:Y6 blends after excitation of D18. We note that energy transfer may provide a secondary charge generation pathway, which would benefit from the very high PLQY of D18[51].

Finally, putting all of these observations together, we propose a model for electron transfer in D18:Y6 films based on our TA results (Supplementary Fig. 1, and Fig. 4c). Exciting D18 produces $^1D_{D18}$ either from direct excitation or ultrafast transfer from $^1LE_{D18}$ (1 and 2). $^1D_{D18}$ then generate free charges $FC_{D18:Y6}$ (3; ~1 ps), partially bypassing the formation of interfacial $^1CT_{D18:Y6}$. In the case of both Y6 and D18 excitation, $FC_{D18:Y6}$ can undergo detrimental back transfer to S_0 via $^1CT_{D18:Y6}$ and $^3T_{Y6}$ (relaxed from $^3CT_{D18:Y6}$) (4–7).

To test this model, we evaluate the electron- and hole-transfer efficiencies (η_{ET}/η_{HT}) derived from TA measurements and compare them with the device IQE (Fig. 3e) in the case of D18- and Y6-selective excitation. By applying our model for the electron-transfer channel, we obtain $\eta_{ET} = 99.5\%$, which is a good match for the IQE_{550} (=97.3%). We propose that this high IQE is due to the slow intrinsic recombination in D18, and fast (τ_{ET}~1 ps), direct transfer of free carriers from D18 to Y6, mostly bypassing the formation of an interfacial $^1CT_{D18:Y6}$ state. The slight deviation between η_{ET} and IQE_{550} may then be due to the formation of a small amount of $^1CT_{D18:Y6}$ or $^3CT_{D18:Y6}$ states. For hole

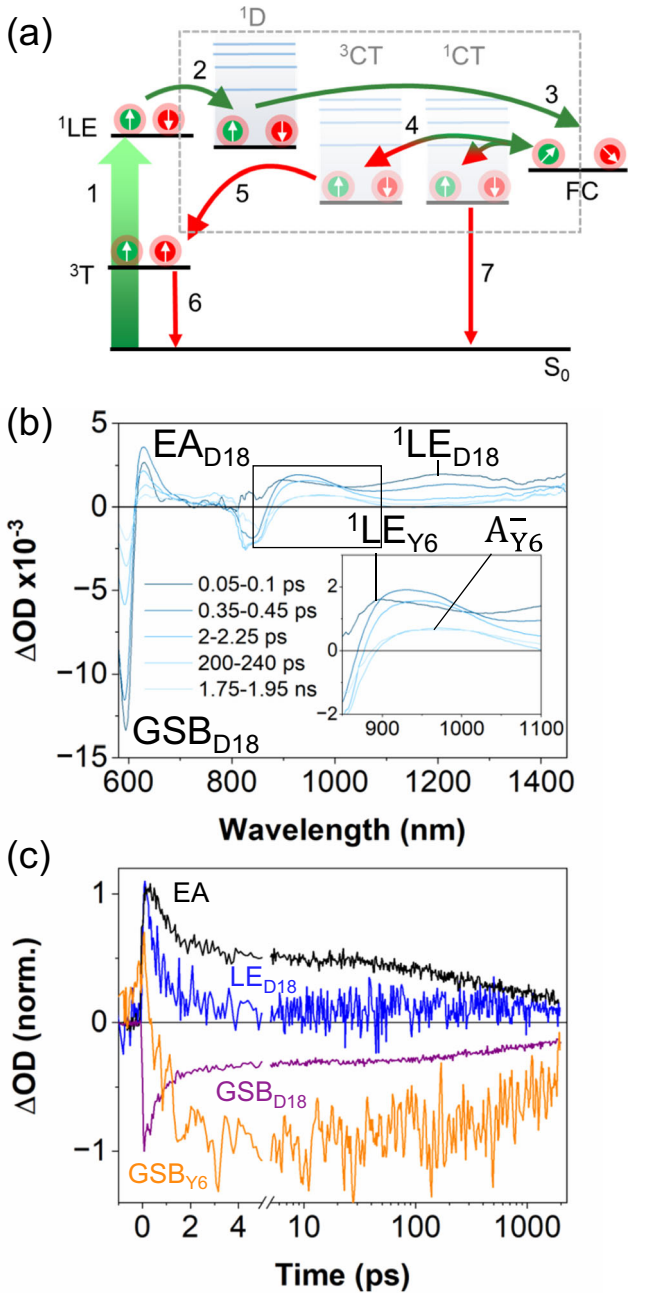

Fig. 4 | TA characterization of a D18:Y6 blend after selective excitation of D18. **a** Proposed charge-separation model in aggregated systems with stronger delocalization character: (1) photoexcitation and ^{1}LE generation; (2) transfer from the ^{1}LE to ^{1}D; (3) transfer from ^{1}D to FC (bypassing interfacial CT states); (4) equilibrium between back transfer to ^{1}CT and ^{3}CT and re-ionization to FC; (5) recombination to the ^{3}T state; (6 and 7) recombination to S_0 from ^{3}T and ^{1}CT. **b** TA spectra of a D18:Y6 blend after selective D18 excitation (550 nm; 2 μJ/cm^2) with the notable features indicated (GSB$_{D18}$/GSB$_{Y6}$: ground-state bleach of D18 or Y6; ^{1}LE$_{D18}$/^{1}LE$_{Y6}$: singlet local exciton of D18 or Y6; EA: electroabsorption peak, A$^-_{Y6}$: Y6 anion). **c** Normalized TA traces of the same D18:Y6 film under the same excitation conditions probed at 595, 650, 860, and 1170 nm for the GSB$_{D18}$, EA, GSB$_{Y6}$, and ^{1}LE$_{D18}$ features, respectively.

transfer following excitation of Y6, we obtain η_{HT} = 92.7%, which is an excellent match for the IQE$_{750}$ (=92.5%). This lower IQE at 750 nm is mostly due to the slower hole injection rate (τ_{HT}~4 ps), and relatively fast LE$_{Y6}$ decay (τ_{LE}~55 ps). As outlined in Supplementary Note 8, we find evidence for CT$_{D18:Y6}$ formation after Y6-selective excitation, contrary to previous reports on similar systems[20]. We note that using the time constant associated with the initial formation of GSB$_{D18}$ (i.e., CT$_{D18:Y6}$ formation; τ_{GSB}~0.4 ps), rather than the generation of EA (i.e., FC formation; τ_{FC}~4 ps), over-estimates the hole-transfer yield (η_{HT} = 99.3%), which is consistent with the active role of the CT$_{D18:Y6}$ intermediate states in the hole-transfer mechanism.

In Supplementary Figs. 35–39, we summarize the TA characterization of charge separation in P3HT:Y6 and PM6:Y6 blends, which we now compare to the case of D18:Y6. We find that P3HT:Y6 is prone to forming ^{1}CT$_{P3HT:Y6}$ states, while PM6:Y6 and D18:Y6 rapidly form free carriers. We propose that the weak interactions in homopolymer donors such as P3HT lead to the formation of strongly bound excitons (E_b = 0.42 eV)[48]. On the other hand, strong π-interactions between polymer chains in aggregated donor polymers such as D18 and PM6 provide the delocalization necessary to reduce the E_b (=0.13 eV for both)[48] and facilitate ultrafast electron transfer and separation. These observations help explain the improved IQE and J_{SC} in OPVs based on D18 and PM6 compared to P3HT (Fig. 3d, e). We further study the recombination kinetics in PM6:Y6 and D18:Y6 blends, where we identify the terminal back recombination in the blend can be reduced when adopting a donor with a stronger delocalization character (Supplementary Note 8).

Discussion

We studied a series of well-known OPV donor polymers: P3HT, PM6, and D18. We first simulated how interchain interactions among different π-moieties in the polymer induce aggregation which alters the extent of excited-state delocalization. Particularly, intimate interchain interactions established between D and A moieties facilitate the through-space delocalization of excitons. We then experimentally revealed the formation of delocalized excitons in strongly π-interacting D18, which dominate the photoluminescence. We found that FC generation in OPV cells adopting a neat D18 or blend absorber largely bypasses the formation of interfacial CT states, which is facilitated by the rapid formation of the luminescent delocalized state in highly ordered D18. This kinetic model, consistent with both the theoretical calculations and ultrafast photophysics, also quantitatively reproduces the measured IQEs of the devices. These findings not only help explain how a PCE of 19.2% is possible for single-junction OPVs but also provide insight into how a strongly delocalized and highly luminescent donor can effectively circumvent the formation of performance-limiting CT states. Designing intimately interacting donor materials with pronounced delocalization character and radiative efficiency could thus be a strategy to maximize the exciton dissociation efficiency while minimizing the terminal back recombination, pushing OPVs forward closer to the Shockley-Queisser limit.

Methods

Materials

D18, T9TBO-F, and Y6-O were synthesized according to literature[45,53,54]. PM6 (Lot no.: YM216A), PffBT4T-2OD (Lot no.: PIA09A), and Y6 was purchased from Solarmer. P3HT (Lot no.: SX9182B) was purchased from 1-Material. Unless mentioned otherwise, all solvents and starting materials were purchased from Sigma–Aldrich, Acros, TCI, and J&K Scientific and used without further purification. The chloroform adduct of tris(dibenzylideneacetone)dipalladium(0) ($Pd_2(dba)_3{\cdot}CHCl_3$) catalyst was prepared according to literature[55]. The tri(*o*-tolyl)phosphine (P(*o*-tol)$_3$) ligand was recrystallized twice from absolute ethanol before use. The abbreviations and full names of chemical structures:

o-DCB: 1,2-dichlorobenzene.

BDT: 2,6-(4,8-bis(5-(2-ethylhexyl-3-fluoro)thiophen-2-yl)-benzo[1,2-*b*:4,5-*b*′]dithiophene).

BDD: bis(2-ethylhexyl)benzo[1′,2′-*c*:4′,5′-*c*′]dithiophene-4,8-dione.

DTBT: dithieno[3′,2′:3,4;2″,3″:5,6]benzo[1,2-*c*][1,2,5]thiadiazole.

P3HT: poly(3-hexylthiophene-2,5-diyl.

PM6: poly[(2,6-(4,8-bis(5-(2-ethylhexyl-3-fluoro)thiophen-2-yl)-benzo[1,2-b:4,5-b′] dithiophene))-alt-(5,5-(1′,3′-di-2-thienyl-5′,7′-bis(2-ethylhexyl)benzo[1′,2′-c:4′,5′-c′] dithiophene-4,8-dione)].

D18: poly[(2,6-(4,8-bis(5-(2-ethylhexyl-3-fluoro)thiophen-2-yl)-benzo[1,2-b:4,5-b′]dithiophene)) -alt-5,5′-(5,8-bis(4-(2-butyloctyl)thiophen-2-yl)dithieno[3′,2′:3,4;2″,3″:5,6]benzo[1,2-c][1,2,5] thiadiazole)].

PffBT4T-2OD: poly[(5,6-difluoro-2,1,3-benzothiadiazol-4,7-diyl)-alt-(3,3‴-di(2-octyldodecyl)-2,2′,5′,2″,5″,2‴-quaterthiophen-5,5‴-diyl)]

C60-G4PA: 2-(2-(2-(2-(4-(1′,5′-dihydro-1′-methyl-2′*H*-[5,6]fullereno-C60-I_h-[1,9-*c*]pyrrol-2′-yl) phenoxy)ethoxy)ethoxy)ethoxy) ethyl-1-phosphonic acid.

Y6: 2,2′-((2Z,2′Z)-((12,13-bis(2-ethylhexyl)-3,9-diundecyl-12,13-dihydro-[1,2,5]thiadiazolo[3,4-e]thieno[2″,3″:4′,5′]thieno[2′,3′:4,5]pyrrolo[3,2-g]thieno[2′,3′:4,5]thieno[3,2-b]indole-2,10-diyl) bis(methanylylidene))bis(5,6-difluoro-3-oxo-2,3-dihydro-1H-indene-2,1-diylidene)) dimalononitrile.

T9TBO-F: 2,2′-((2Z,2′Z)-((12,13-bis(2-butyloctyl)-3,9-dinonyl-12,13-dihydro-[1,2,5]thiadiazolo [3,4-e]thieno[2″,3″:4′,5′]thieno[2′,3′:4,5]pyrrolo[3,2-g]thieno[2′,3′:4,5]thieno[3,2-b]indole-2,10-diyl)bis(methanylylidene))bis(5,6-difluoro-3-oxo-2,3-dihydro-1H-indene-2,1-diylidene)) dimalononitrile.

Y6-O: 2,2′-((2Z,2′Z)-((12,13-bis(2-butyloctyl)-3,9-didodecyloxyl-12,13-dihydro-[1,2,5] thiadiazolo[3,4-e]thieno[2″,3″:4′,5′]thieno[2′,3′:4,5] pyrrolo[3,2-g]thieno[2′,3′:4,5]thieno[3,2-b] indole-2,10-diyl)bis(methanylylidene))bis(5,6-difluoro-3-oxo-2,3-dihydro-1H-indene-2,1-diylidene)) dimalononitrile.

Polymerization of D18

In an oven-dried Schlenk tube was added 2,6-bis(trimethytin)-4,8-bis(5-(2-ethylhexyl)-4-fluorothiophen-2-yl)benzo[1,2-b:4,5-b′]dithiophene (0.1 mmol), 5,8-bis(5-bromo-4-(2-butyloctyl)thiophen-2-yl) dithieno[3′,2′:3,4;2″,3″:5,6]benzo[1,2-*c*][1,2,5]thiadiazole (0.1 mmol), $Pd_2(dba)_3{\cdot}CHCl_3$ (3 mol%) and P(*o*-tol)$_3$ (6 mol%). The Schlenk tube was then transferred into an N_2-filled glovebox and 12 mL dry toluene was added to fully dissolve the precursors. After carefully sealing the Schlenk tube, the reaction mixture was heated to reflux for 4 h and then precipitated into cold methanol. The crude was collected by filtration and loaded into a Soxhlet thimble which was then successively extracted with methanol, acetone, THF, chloroform, and chlorobenzene. The chlorobenzene fraction was collected (81 mg, yield: 60%).

Gel permeation chromatography

The number-average molecular weight (M_n) and polydispersity ($Đ$) of P3HT, PM6, and D18 were determined by an Agilent 1260 Infinity II High-Temperature Gel Permeation Chromatography System calibrated with polystyrene standards, using *o*-DCB as the mobile phase eluted at 130 °C. P3HT: M_n = 51.9 kDa, $Đ$ = 2.60; PM6: M_n = 40.3 kDa, $Đ$ = 4.06; D18: M_n = 68.5 kDa, $Đ$ = 2.17.

Optical properties characterizations

The UV-vis-NIR absorption spectra of polymer or blend spin-cast on quartz substrates were recorded on a Shimadzu 1700 UV-Vis Spectrometer. The thicknesses of the films are 55 ± 2 nm for neat polymer films, and 105 ± 3 nm for blends as measured from a Bruker Dektak XT stylus profilometer. The photoluminescence (PL) spectra and the corresponding PL quantum yield (PLQY) of thin-film samples spin-cast on quartz substrates were recorded with a QE-Pro Spectrometer equipped with an integrating sphere using a 365 nm laser as the excitation source. Temperature-dependent PL spectra of the polymer sample in solution (10 μg/mL in *o*-DCB) were recorded with an FLS920 Spectrometer (Edinburgh Instruments) with an integrated heating module.

Photovoltaic cells fabrication

Pre-patterned ITO-coated glass with a sheet resistance of ~15 Ω/sq was cleaned by sonication sequentially in detergent, DI water, acetone, and isopropanol, each for 30 min. The substrates were then dried under 80 °C overnight in an oven, and treated with plasma for 30 min before usage. The OPV cells adopting neat donor polymer (P3HT, PM6, and D18) were fabricated based on an inverted (n-i-p) architecture of ITO/C60-G4PA/polymer/MoO_3/Ag. A solution of C60-G4PA and an *n*-dopant, Bis-C60 (9.3:1 *w/w*, total concentration 1.5 mg/mL)[56], dissolved in a mixed solvent of 2-isopropanol/chlorobenzene (1:4 *v/v*) with 8% chloronaphthalene as an additive, was deposited onto ITO substrate through spin-coating at 2300 r.p.m. in a nitrogen-filled glovebox. The substrate was then annealed at 120 °C and then rinsed with a mixed solvent of 2-isopropanol/chlorobenzene (1:4 *v/v*) to remove extra SAM molecules. The donor polymer was then spin-cast on top, and the thickness of the polymer layer was optimized according to cell performances (P3HT: ~25 nm; PM6: ~40 nm; D18: ~40 nm). P3HT was dissolved in chloroform at a concentration of 6 mg/mL and stirred for 1 h prior to usage. PM6 was dissolved in chloroform at a concentration of 6 mg/mL and stirred for at least 2 h prior to usage. D18 was dissolved in chlorobenzene/carbon disulfide (3:2 *v/v*) at a concentration of 4.5 mg/mL and stirred for at least 2 h prior to usage to ensure the materials were fully dissolved. For OPV cells adopting a D18:$PC_{71}BM$ active layer, the devices were fabricated in an inverted (n-i-p) configuration of ITO/C60-G4PA/D18:$PC_{71}BM$/MoO_3/Ag. D18 and $PC_{71}BM$ (1:1.6 *w/w*) were dissolved in chlorobenzene/carbon disulfide (3:2 *v/v*) at a total concentration of 9.36 mg/mL and stirred for at least 2 h prior to spin-casting (2800 r.p.m.) to ensure the materials are fully dissolved. After the deposition of the active layer, the MoO_3 (~6 nm) and Ag (~100 nm) top electrodes were thermally evaporated at 5×10^{-5} Pa through a shadow mask, which was used to define the dimension of the device area as a rectangle of 2.8 × 2.3 mm^2.

The OPV cells adopting a donor:acceptor blend were fabricated based on a conventional (p-i-n) architecture of ITO/PEDOT:PSS/polymer:Y6/PNDIT-F3N/Ag. PEDOT:PSS (Heraeus *CLEVIOS*™ P VP AI 4083) was spin-cast at 4500 r.p.m., and then annealed at 120 °C for 15 min in dry air. The deposition of active layers was optimized according to the best fabrication conditions. For D18 and Y6 (1:1.6 *w/w*) were dissolved in chloroform at a total concentration of 15.6 mg/mL, and stirred for 1 h at 60 °C. The warm solution was then spin-cast onto the substrate at 2500 r.p.m. for 40 s. For the mixture of PM6 and Y6 (1:1.2 *w/w*) was dissolved in chloroform/2-chloronaphthalene (200:1 *v/v*) at a total concentration of 15.4 mg/mL at 50 °C and stirred for at least 2 h prior to usage to ensure the materials are fully dissolved. After cooling down, the solution was then spin-cast onto the substrate at 2500 r.p.m. for 40 s, following annealing at 100 °C for 5 min. For P3HT and Y6 (1:1 *w/w*) were dissolved in tetrahydrofuran at a total concentration of 14 mg/mL, and stirred for 1 h at room temperature. Then, the solution was spin-cast onto the substrate at 2500 r.p.m. for 40 s. A thin layer of PNDIT-F3N (0.5–1 mg/mL in methanol) was then coated on top of the active layer. Finally, a layer of Ag (~220 nm) as the top electrode was thermally evaporated at 5×10^{-5} Pa at a rate between 2.5 and 5 Å s^{-1} through a shadow mask, which was used to define the dimension of the device area as a rectangle of 2.8 × 2.3 mm^2.

Photovoltaic cells characterizations

The current density-voltage characteristics were recorded using a Keithley 2400 Source Meter Unit and measured under AM1.5G (100 mW/cm^2) irradiation using an EnliTech SS-F5 solar simulator in an N_2-filled glovebox with the environmental temperature maintained at ~25 °C. The light intensity was calibrated using a standard silicon solar cell (with a KG-2 filter) from NREL to bring spectral mismatch to unity. The active area of the cells was defined by a non-reflective metal mask with an aperture area of 4 mm^2, which is aligned with the rectangular device area. EQE spectra were collected using an Enlitech QE-S EQE system equipped with a standard Si diode.

Quasi-steady-state photovoltaic performance measurement

The certification of the D18:T9TBO-F:Y6-O ternary cell (Newport Calibration Cert. # 2502) was performed at an accredited laboratory (MKS Instruments/Newport PV Lab, Bozeman, MT, USA) through a 10-point *I*–*V* sweep configuration, wherein the bias voltage (or current for V_{OC} determination) is held constant until the measured current (or voltage for V_{OC}) is determined to be fluctuating within 0.07% level. The result is intended to represent the quasi-steady-state performance of the device. The duration of the 10-point *I*–*V* measurement is approximately 7 min.

Molecular dynamics (MD) calculation

MD force field parameter optimization. The MD simulation was performed using Gromacs 2021 package[57]. To construct appropriate polymer force field parameters, the following steps were undertaken:

(a) DFT Optimization: We started by optimizing the geometries of the D18/PM6/P3HT polymer 3-mer using Gaussian 16 at the PBE0-D3BJ/def2SVP level.

(b) Initial Topology Generation: The optimized 3-mer topology file was generated using ztop with the command:

$$ztop.py\text{-}g''3mer.\log''\text{-}r\ e$$

This step includes three sub-steps:

(1) Initial force field generation based on GAFF2 using AmberTools.
(2) Calculation of RESP2 charges for all atoms using Multiwfn[60].
(3) Replacement of force field parameters (equilibrium bond lengths and angles) with those from the DFT-optimized structure.

(c) Fragmentation and Reassembly: After generating the 3-mer topology file, we fragmented it into smaller segments. The fragmentation was performed using the following command:

$$ztop.py\text{-}f\ ''D;p=3mer.top;x=3mer.gro;site=D12{:}11\text{-}22,$$
$$D11{:}8-21;resname=DON''-savelib$$

This command will generate a fragment named "*D*"

D12:11-22 specifies the site name and atom indices for the bond to be cut.

Various segments such as alkyl chains (R), donor (*D*), and acceptor (*A*) were obtained.

These fragments were then reassembled into a hexamer using ztop using the following command:

$$ztop.py-loadlib\text{-}bHR[ADRR]5TR\text{-}opoly.top,poly.pdb$$

(d) Dihedral Potential Fitting: Dihedral potentials were fitted using ztop with the command:

$$ztop.py\text{-}pPPI.top\text{-}xPPI.gro\text{-}d8\text{-}15$$

PPI is the segment containing the dihedral angle of interest.
8-15 specifies the bond indices for the dihedral.
This fitting process includes:

(1) Generation of Gaussian input files with various dihedral angles.
(2) Energy calculations for these structures.
(3) Least-squares fitting to obtain the corresponding dihedral parameters.

(e) Parameter Transfer to Polymer Topology: The obtained dihedral parameters were transferred to the polymer topology file using:

$$ztop.py\text{-}f''S;p=PPI.top;x=PPI.gro''\text{-}ppoly.top\text{-}xpoly.pdb\text{-}ts'';$$
$$m=1-2,7-9,15-19,29,38-39;a=7-9,15-16,19;p=d''$$

m = specifies the matching atom indices.
a = specifies the atom indices for parameter transfer.
p = d indicates the transfer of dihedral parameters.

This comprehensive approach ensured that the force field parameters used in our MD simulations were accurately derived from high-level quantum chemical calculations, providing reliable and robust simulations of the polymer dynamics.

MD system construction and simulation

The simulated polymer films were constructed using the following procedure. First, 30 × D18 6-mers or 30 × PM6 6-mers or 30 × P3HT 30-mers were randomly placed into a rectangle box with edge lengths of 20 × 20 × 20 nm using packmol[58]. The NPT run was performed for 20 ns with 5 annealing cycles between 500 K and 300 K. During the annealing, isotropic Berendsen barostat was used. Finally, the production NPT run was performed at 300 K for 10 ns to obtain the trajectories. All MD simulations were employed with a velocity-Verlet integrator at 2.0 fs time step with LINCS algorithm to constrain bonds with hydrogen. The temperature was controlled with a V-rescale thermostat. The pressure was controlled using Berendsen barostat. Three independent simulations were performed for each system. The analysis was performed on the frames extracted from the 10 ns production run with a 200 ps interval.

Close-contact number analysis

The close-contact number is defined by the average number of close-contact atoms in a specific molecular moiety over another. Homopolymer (P3HT) is divided into π (π-bridge), and R (alkyl chain) moieties. Copolymers (PM6 and D18) are divided into *D* (electron-donating moiety), *A* (electron-accepting moiety), π (π-bridge), and R (alkyl chain) moieties. Heavy atoms (non-hydrogen atoms) within a distance of 3.5 Å to each other are defined as "close contacts" for all moieties. The statistics of neighboring moieties was then summed over all the 150 frames from three trajectories followed by classification according to the correlating moieties. The analysis was performed using MDAnalysis package[59].

Density functional theory (DFT) calculation

The interchain interactions and corresponding exciton distribution were simulated via stacking two polymer segments with various configurations: π-bridge from one polymer segment onto π-bridge from another for P3HT ($n = 6$), and *D* or *A* moiety from one polymer segment onto *D* or *A* moiety from another for PM6 and D18 ($n = 1$). All optimizations were done at PBE0/def2SVP level with Grimme's D3BJ empirical dispersion correction[60]. Then the adiabatic excited states were calculated at the same level as TDDFT. PCM solvation models were used with diphenylether as a solvent in all the calculations to simulate the dielectric environment of a solid. All the calculations are performed using the Gaussian 16 program[61]. The electron-hole distribution analysis was performed using the Multiwfn program[62].

Organic light-emitting diode fabrication and characterizations

The devices were fabricated in an architecture of ITO/PEDOT:PSS/D18/B3PYMPM/LiF/Al. The patterned ITO-coated glasses were ultrasonically cleaned in detergent solution, deionized water, acetone, isopropyl alcohol, and ethanol, each for 20 min, respectively, and then dried under compressed N_2 flow. The substrates were further cleaned with Plasma cleaner (Harrick, PDC-002-HP) for 5 min before use. A hole-transporting layer (HTL) was prepared by spin-coating PEDOT:PSS (Heraeus *CLEVIOS*™ P VP AI 4083) at 4000 r.p.m. for 40 s, and annealed at 150 °C for 15 min in ambient air. After cooling to room temperature, the substrates were transferred into an N_2-filled glovebox. For the emitting layer, 30 µL precursor solution (6 mg/mL D18 in chlorobenzene heated at 80 °C, stirred for 2 h before use) was spin-coated on top of HTL at 2000 r.p.m. for 40 s. Finally, a 50-nm-thick layer of B3PYMPM, a 2-nm-thick layer of LiF, and a 60-nm-thick layer of Al were deposited using a thermal evaporation system under a vacuum

of <1.0 × 10^{-4}Pa. The active area was 3 mm^2 (2 mm × 1.5 mm), which was defined by the overlapping area of ITO and Al electrodes. All devices were measured in an N_2-filled glovebox, using a Keithley 2400 Source Meter and a QE-Pro Spectrometer.

Transient absorption spectroscopy

Samples used in TA experiments were prepared using the protocol identical to photovoltaic cell fabrication and were epoxy-sealed in N_2 glovebox. The pump pulse was generated via Coherent Inc./Light Source OPerA optical parametric amplifier from a fraction of the output (800 nm, 50 fs, 1 kHz) of a Coherent Libra Ti:Sapphire amplifier. The other fraction of the amplifier output was focused onto CaF_2 or sapphire crystals to generate the supercontinuum probe pulse. The probe beam was spectrally aligned with the pump on the sample. The sample was excited with either a 550 nm or 750 nm laser pulse, where an appropriate band pass filter was used to obtain a narrow laser profile centered at the excitation wavelength of choice. The laser beam profile was measured at the sample position using a Thorlabs CCD camera beam profiler (BC106N-VIS) to ensure the irradiation had a Gaussian profile and to calculate the irradiation area. The pump excitation fluence per pulse was calculated based on average power measured with the Coherent FieldMater laser power meter, the beam diameter obtained from the Thorlabs beam profiler software (~0.7 mm, $1/e^2$ cut-off), and pulse frequency (1 kHz). Signals were detected using a CMOS and InGaAs fiber optics-coupled photodiode array spectrometer. The pump-probe delay of up to 2 ns was set using a mechanical translational stage. Data was taken in random order of pump-probe delay to avoid the influence of laser power fluctuation during the scan and was collected using HELIOS software (Ultrafast). The instrumental response function (IRF) of the TA set-up was measured using a thin glass substrate. We chose a low fluence of 2 μJ/cm^2 (2 mW/cm^2), first to ensure that we were below the limit of non-linear photophysics such as two-photon absorption, as well as exciton-exciton and exciton-charge annihilation (Supplementary Fig. 9). Second, using this fluence allowed us to probe excited-state dynamics in a limit that is more relevant to the working conditions of a typical OPV cell (~10^{17} excitations/cm^{-3}).

Time-resolved photoluminescence

Time-resolved PL spectra were collected using a Hamamatsu streak camera with a synchroscan unit. The same samples used in the TA measurement were irradiated with an 810 nm pulse pumped at 1 kHz from a Coherent Inc./Light Source OPerA optical parametric amplifier. The excitation density was matched to the TA measurement. The IRF of the tr-PL set-up was measured with a sanded-glass sample in the same optical geometry as the sample measurements.

Small-angle X-ray scattering (SAXS) measurements

SAXS experiments were performed at the 16-ID beamline of the National Synchrotron Light Source II at Brookhaven National Laboratory to probe the Q ranges of 0.006 < Q < 3 $Å^{-1}$ using multiple Pilatus detectors[63]. The samples were measured using a 1.5 mm diameter quartz capillary. Before solution scattering measurements were performed, both empty cells and blank solvents were measured for proper background subtraction. For each measurement, 10–20 repeated measurements were taken on various parts of the sample using X-ray energy at 13.5 keV with a 1 s exposure time to avoid beam damage. The scattering profiles were then obtained by averaging the repeated measurements and subtracting the empty cell and blank solvent contributions using a Python package py4xs in Jupyter Notebooks[64]. The model fitting of the scattering profile was performed using the Guinier-Porod model in the SasView program.

Reporting summary

Further information on research design is available in the Nature Portfolio Reporting Summary linked to this article.

Data availability

The datasets generated and/or analyzed during the current study are available from the corresponding authors upon request.

References

1. Gregg, B. A. Excitonic solar cells. *J. Phys. Chem. B* **107**, 4688–4698 (2003).
2. Zhang, G. et al. Renewed prospects for organic photovoltaics. *Chem. Rev.* **122**, 14180–14274 (2022).
3. Rao, A., Gillett, A. J. & Friend, R. H. Engineering the spin-exchange interaction in organic semiconductors. *Nat. Mater.* **21**, 976–978 (2022).
4. Azzouzi, M. et al. Reconciling models of interfacial state kinetics and device performance in organic solar cells: impact of the energy offsets on the power conversion efficiency. *Energy Environ. Sci.* **15**, 1256–1270 (2022).
5. Tang, C. W. Two-layer organic photovoltaic cell. *Appl. Phys. Lett.* **48**, 183–185 (1986).
6. Clarke, T. M. & Durrant, J. R. Charge photogeneration in organic solar cells. *Chem. Rev.* **110**, 6736–6767 (2010).
7. Lowrie, W. et al. Organic photovoltaics: the current challenges. *J. Chem. Phys.* **158**, 110901 (2023).
8. Rao, A. et al. The role of spin in the kinetic control of recombination in organic photovoltaics. *Nature* **500**, 435–439 (2013).
9. Liu, Y., Zheng, Z., Coropceanu, V., Brédas, J.-L. & Ginger, D. S. Lower limits for non-radiative recombination loss in organic donor/acceptor complexes. *Mater. Horiz.* **9**, 325–333 (2022).
10. Benduhn, J. et al. Intrinsic non-radiative voltage losses in fullerene-based organic solar cells. *Nat. Energy* **2**, 17053 (2017).
11. Chen, X.-K. et al. A unified description of non-radiative voltage losses in organic solar cells. *Nat. Energy* **6**, 799–806 (2021).
12. Hinrichsen, T. F. et al. Long-lived and disorder-free charge transfer states enable endothermic charge separation in efficient non-fullerene organic solar cells. *Nat. Commun.* **11**, 5617 (2020).
13. Jiang, K. et al. Suppressed recombination loss in organic photovoltaics adopting a planar–mixed heterojunction architecture. *Nat. Energy* **7**, 1076–1086 (2022).
14. Sulas, D. B. et al. Open-circuit voltage losses in selenium-substituted organic photovoltaic devices from increased density of charge-transfer states. *Chem. Mater.* **27**, 6583–6591 (2015).
15. Gélinas, S. et al. Ultrafast long-range charge separation in organic semiconductor photovoltaic diodes. *Science* **343**, 512–516 (2014).
16. Tamai, Y. et al. Ultrafast long-range charge separation in non-fullerene organic solar cells. *ACS Nano* **11**, 12473–12481 (2017).
17. Price, M. B. et al. Free charge photogeneration in a single component high photovoltaic efficiency organic semiconductor. *Nat. Commun.* **13**, 2827 (2022).
18. Zhang, G. et al. Delocalization of exciton and electron wavefunction in non-fullerene acceptor molecules enables efficient organic solar cells. *Nat. Commun.* **11**, 3943 (2020).
19. Xu, J. et al. The molecular ordering and double-channel carrier generation of nonfullerene photovoltaics within multi-length-scale morphology. *Adv. Mater.* **34**, 2108317 (2022).
20. Wang, R. et al. Charge separation from an intra-moiety intermediate state in the high-performance PM6:Y6 organic photovoltaic blend. *J. Am. Chem. Soc.* **142**, 12751–12759 (2020).
21. Song, Y. et al. Mechanistic study of charge separation in a non-fullerene organic donor–acceptor blend using multispectral multidimensional spectroscopy. *J. Phys. Chem. Lett.* **12**, 3410–3416 (2021).
22. Wei, Y.-C. et al. Overcoming the energy gap law in near-infrared OLEDs by exciton–vibration decoupling. *Nat. Photonics* **14**, 570–577 (2020).
23. Zhu, L. et al. Small exciton binding energies enabling direct charge photogeneration towards low-driving-force organic solar cells. *Angew. Chem. Int. Ed.* **60**, 15348–15353 (2021).

24. Dong, Y. et al. Orientation dependent molecular electrostatics drives efficient charge generation in homojunction organic solar cells. *Nat. Commun.* **11**, 4617 (2020).
25. Yi, F. et al. Non-fully conjugated dimerized giant acceptors with different alkyl-linked sites for stable and 19.13% efficiency organic solar cells. *Angew. Chem. Int. Ed.* **63**, e202319295 (2024).
26. Zeng, R. et al. Achieving 19% efficiency in non-fused ring electron acceptor solar cells via solubility control of donor and acceptor crystallization. *Nat. Energy* **9**, 1117–1128 (2024).
27. Lu, H. et al. High-pressure fabrication of binary organic solar cells with high molecular weight D18 yields record 19.65% efficiency. *Angew. Chem. Int. Ed.* **62**, e202314420 (2023).
28. Wang, Z. et al. Thermodynamic properties and molecular packing explain performance and processing procedures of three D18:NFA organic solar cells. *Adv. Mater.* **32**, 2005386 (2020).
29. Ghosh, S., Das, S., Kumar, N. R., Agrawal, A. R. & Zade, S. S. Effect of heteroatom (S/Se) juggling in donor–acceptor–donor (D–A–D) fused systems: synthesis and electrochemical polymerization. *N. J. Chem.* **41**, 11568–11575 (2017).
30. Kato, S.-I. et al. π-Extended thiadiazoles fused with thienopyrrole or indole moieties: synthesis, structures, and properties. *J. Org. Chem.* **77**, 7595–7606 (2012).
31. Coffin, R. C., Peet, J., Rogers, J. & Bazan, G. C. Streamlined microwave-assisted preparation of narrow-bandgap conjugated polymers for high-performance bulk heterojunction solar cells. *Nat. Chem.* **1**, 657–661 (2009).
32. Ziffer, M. E. et al. Tuning H- and J-aggregate behavior in π-conjugated polymers via noncovalent interactions. *J. Phys. Chem. C* **122**, 18860–18869 (2018).
33. Ziffer, M. E. et al. Long-lived, non-geminate, radiative recombination of photogenerated charges in a polymer/small-molecule acceptor photovoltaic blend. *J. Am. Chem. Soc.* **140**, 9996–10008 (2018).
34. Vachova, L., Novakova, V., Kopecky, K., Miletin, M. & Zimcik, P. Effect of intramolecular charge transfer on fluorescence and singlet oxygen production of phthalocyanine analogues. *Dalton Trans.* **41**, 11651–11656 (2012).
35. Reid, O. G., Pensack, R. D., Song, Y., Scholes, G. D. & Rumbles, G. Charge photogeneration in neat conjugated polymers. *Chem. Mater.* **26**, 561–575 (2014).
36. Balzer, D. & Kassal, I. Mechanism of delocalization-enhanced exciton transport in disordered organic semiconductors. *J. Phys. Chem. Lett.* **14**, 2155–2162 (2023).
37. Shaw, P. E., Ruseckas, A. & Samuel, I. D. W. Exciton diffusion measurements in poly(3-hexylthiophene). *Adv. Mater.* **20**, 3516–3520 (2008).
38. Cha, H. et al. Influence of blend morphology and energetics on charge separation and recombination dynamics in organic solar cells incorporating a nonfullerene acceptor. *Adv. Funct. Mater.* **28**, 1704389 (2018).
39. Firdaus, Y. et al. Long-range exciton diffusion in molecular non-fullerene acceptors. *Nat. Commun.* **11**, 5220 (2020).
40. Weu, A. et al. Field-assisted exciton dissociation in highly efficient PffBT4T-2OD:fullerene organic solar cells. *Chem. Mater.* **30**, 2660–2667 (2018).
41. Hu, H. et al. Design of donor polymers with strong temperature-dependent aggregation property for efficient organic photovoltaics. *Acc. Chem. Res.* **50**, 2519–2528 (2017).
42. Liu, Y. et al. Aggregation and morphology control enables multiple cases of high-efficiency polymer solar cells. *Nat. Commun.* **5**, 5293 (2014).
43. Noone, K. M. et al. Photoinduced charge transfer and polaron dynamics in polymer and hybrid photovoltaic thin films: organic vs inorganic acceptors. *J. Phys. Chem. C* **115**, 24403–24410 (2011).
44. Eisner, F. et al. Emissive charge-transfer states at hybrid inorganic/organic heterojunctions enable low non-radiative recombination and high-performance photodetectors. *Adv. Mater.* **34**, 2104654 (2022).
45. Liu, Q. et al. 18% Efficiency organic solar cells. *Sci. Bull.* **65**, 272–275 (2020).
46. Yuan, J. et al. Single-junction organic solar cell with over 15% efficiency using fused-ring acceptor with electron-deficient core. *Joule* **3**, 1140–1151 (2019).
47. Gao, M. et al. Thermally stable poly(3-hexylthiophene): non-fullerene solar cells with efficiency breaking 10. *Aggregate* **3**, e190 (2022).
48. Bertrandie, J. et al. The energy level conundrum of organic semiconductors in solar cells. *Adv. Mater.* **34**, 2202575 (2022).
49. Balzer, D. & Kassal, I. Even a little delocalization produces large kinetic enhancements of charge-separation efficiency in organic photovoltaics. *Sci. Adv.* **8**, eabl9692 (2022).
50. Bakulin, A. A. et al. The role of driving energy and delocalized states for charge separation in organic semiconductors. *Science* **335**, 1340–1344 (2012).
51. Karuthedath, S. et al. Intrinsic efficiency limits in low-bandgap non-fullerene acceptor organic solar cells. *Nat. Mater.* **20**, 378–384 (2021).
52. Carr, J. M., Gish, M. K., Reid, O. G. & Rumbles, G. Missing excitons: how energy transfer competes with free charge generation in dilute-donor/acceptor systems. *ACS Energy Lett.* **9**, 896–907 (2024).
53. Gao, W. et al. Asymmetric acceptors enabling organic solar cells to achieve an over 17% efficiency: conformation effects on regulating molecular properties and suppressing nonradiative energy loss. *Adv. Energy Mater.* **11**, 2003177 (2021).
54. Chen, Y. et al. Alkoxy substitution on IDT-Series and Y-Series non-fullerene acceptors yielding highly efficient organic solar cells. *J. Mater. Chem. A* **9**, 7481–7490 (2021).
55. Zalesskiy, S. S. & Ananikov, V. P. Pd2(dba)3 as a precursor of soluble metal complexes and nanoparticles: determination of palladium active species for catalysis and synthesis. *Organometallics* **31**, 2302–2309 (2012).
56. Li, C.-Z. et al. Effective interfacial layer to enhance efficiency of polymer solar cells via solution-processed fullerene-surfactants. *J. Mater. Chem.* **22**, 8574–8578 (2012).
57. Abraham, M. J. et al. GROMACS: high performance molecular simulations through multi-level parallelism from laptops to supercomputers. *Softwarex* **1-2**, 19–25 (2015).
58. Martínez, L., Andrade, R., Birgin, E. G. & Martínez, J. M. PACKMOL: a package for building initial configurations for molecular dynamics simulations. *J. Comput. Chem.* **30**, 2157–2164 (2009).
59. Michaud-Agrawal, N., Denning, E. J., Woolf, T. B. & Beckstein, O. MDAnalysis: a toolkit for the analysis of molecular dynamics simulations. *J. Comput. Chem.* **32**, 2319–2327 (2011).
60. Grimme, S., Ehrlich, S. & Goerigk, L. Effect of the damping function in dispersion corrected density functional theory. *J. Comput. Chem.* **32**, 1456–1465 (2011).
61. Frisch, M. J. et al. *Gaussian 16 Rev. C. 01* (Gaussian Inc., 2016).
62. Lu, T. & Chen, F. Multiwfn: a multifunctional wavefunction analyzer. *J. Comput. Chem.* **33**, 580–592 (2012).
63. Yang, L., Liu, J., Chodankar, S., Antonelli, S. & DiFabio, J. Scanning structural mapping at the Life Science X-ray Scattering Beamline. *J. Synchrotron Radiat.* **29**, 540–548 (2022).
64. Yang, L. et al. Solution scattering at the Life Science X-ray Scattering (LiX) beamline. *J. Synchrotron Radiat.* **27**, 804–812 (2020).

Acknowledgements

This work was primarily supported by the Office of Naval Research (N00014-20-1-2191) which supported the development of efficient organic donor polymers and non-fullerene acceptors as well as the transient absorption spectroscopy, time-resolved PL, and all

contributions to experimental design, analysis, and writing by R.J.E.W. and D.S.G. A.K.Y.J. thanks the sponsorship of the Lee Shau-Kee Chair Professor (Materials Science) for career development and mentoring of faculty in CityU, the APRC Grant of the City University of Hong Kong (9380086) is a start-up fund that supported the establishment and infrastructure maintenance of the synthetic and optoelectronic characterization facility of JEN group, Innovation and Technology Fund (GHP/018/20SZ) which supported the development of solar windows by combining commercial D18-based OPV with low-E glasses, and Guangdong-Hong Kong-Macao Joint Laboratory of Optoelectronic and Magnetic Functional Materials (2019B121205002) which supported the workshop and travel and visits of researchers between CityU and SCUT to promote collaborations. F.R.L. acknowledges the support of the Postdoctoral Fellowship Scheme from the Research Grants Council of Hong Kong (CityU PDFS2122-1S06). D.S.G. and R.J.E.W. acknowledge private funding from the Washington Research Foundation endowment, the Alvin L. and Verla R. Kwiram endowment, and the B. Seymour Rabinovich Endowment for providing supplemental salary support and maintaining the research infrastructure which made this work possible. R.J.E.W. also acknowledges support from the Momental Foundation via the Mistletoe Research Fellowship. The authors also gratefully acknowledge Dr. Z. Peng and Prof. H. Ade from North Carolina State University; Dr. J. Yan, Prof. J. Nelson and other group members from the Imperial College London; Prof. S.B. Jo from Sungkyunkwan University; Prof. C. Zhang from Nanjing University; Tim Pollock of the University of Washington Molecular Analysis Facility; and Kristine Parra of the University of Washington, for their experimental assistance and/or insightful discussions. Open Access made possible with partial support from the Open Access Publishing Fund of the City University of Hong Kong.

Author contributions

K.J., R.J.E.W., F.R.L., D.S.G., and A.K.Y.J. conceived the project and designed the experiments. K.J. and T.X. fabricated and characterized the photovoltaic cells. R.J.E.W. conducted TA and streak PL experiments and corresponding analysis. C.Z. conducted the computational study. J.L., Y.L., and Z.W. conducted PLQY and temperature-dependent PL experiments, and fabricated and characterized the light-emitting diodes of D18. A.K. and Y.D. performed the solution-state SAXS characterizations. K.L. and F.R.L. synthesized and/or characterized the materials. K.J., R.J.E.W, and F.R.L. wrote the manuscript with input from S.H.J., J.Z., and H.L.Y., and the manuscript was approved by all authors. A.K.Y.J., D.S.G., and F.R.L. supervised the study and revised the manuscript.

Competing interests

The authors declare no competing interests.

Additional information

Supplementary information The online version contains supplementary material available at https://doi.org/10.1038/s41467-025-58352-x.

Correspondence and requests for materials should be addressed to Francis R. Lin, David S. Ginger or Alex K.-Y. Jen.

Peer review information *Nature Communications* thanks the anonymous, reviewer(s) for their contribution to the peer review of this work. A peer review file is available.

Reprints and permissions information is available at http://www.nature.com/reprints

Publisher's note Springer Nature remains neutral with regard to jurisdictional claims in published maps and institutional affiliations.

[1]Department of Chemistry, City University of Hong Kong, Kowloon, Hong Kong. [2]Department of Chemistry, University of Washington, Seattle, WA, USA. [3]Department of Materials Science and Engineering, City University of Hong Kong, Kowloon, Hong Kong. [4]Department of Chemistry, Wuhan University, Wuhan, Hubei, China. [5]Xiamen Key Laboratory of Optoelectronic Materials and Advanced Manufacturing, Institute of Luminescent Materials and Information Displays, College of Materials Science and Engineering, Huaqiao University, Xiamen, Fujian, China. [6]Department of Chemical & Biomolecular Engineering, University of Illinois Urbana-Champaign, Urbana, IL, USA. [7]Hong Kong Institute for Clean Energy (HKICE), City University of Hong Kong, Kowloon, Hong Kong. [8]Department of Materials Science and Engineering, University of Washington, Seattle, WA, USA. [9]Center for Photonics Information and Energy Materials, Shenzhen Institutes of Advanced Technology, Chinese Academy of Sciences, Shenzhen, Guangdong, China. [10]State Key Laboratory of Marine Pollution (SKLMP), City University of Hong Kong, Kowloon, Hong Kong. [11]These authors contributed equally: Kui Jiang, Robert J. E. Westbrook. ✉e-mail: franclin@cityu.edu.hk; dginger@uw.edu; alexjen@cityu.edu.hk